ACS APPLIED MATERIALS & INTERFACES

www.acsami.org

Research Article

Aggregation Reduces Subcellular Localization and Cytotoxicity of Single-Walled Carbon Nanotubes

Mitchell Gravely, Aidan Kindopp, Lauren Hubert, Matthew Card, Aceer Nadeem, Christopher Miller, and Daniel Roxbury*

Cite This: https://doi.org/10.1021/acsami.2c02238

Read Online

ACCESS | Metrics & More | Article Recommendations | Supporting Information

ABSTRACT: The non-covalent biomolecular functionalization of fluorescent single-walled carbon nanotubes (SWCNTs) has resulted in numerous *in vitro* and *in vivo* sensing and imaging applications due to many desirable optical properties. In these applications, it is generally presumed that pristine, singly dispersed SWCNTs interact with and enter live cells at the so-called nano-biointerface, for example, the cell membrane. Despite numerous fundamental studies published on this presumption, it is known that nanomaterials have the propensity to aggregate in protein-containing environments before ever contacting the nano-biointerface. Here, using DNA-functionalized SWCNTs with defined degrees of aggregation as well as near-infrared hyperspectral microscopy and toxicological assays, we show that despite equal rates of internalization, initially aggregated SWCNTs do not further accumulate within individual subcellular locations. In addition to subcellular accumulations, SWCNTs initially with a low degree of aggregation can induce significant deleterious effects in various long-term cytotoxicity and real-time proliferation assays, which are markedly different when compared to those of SWCNTs that are initially aggregated. These findings suggest the importance of the aggregation state as a critical component related to intracellular processing and toxicological response of engineered nanomaterials.

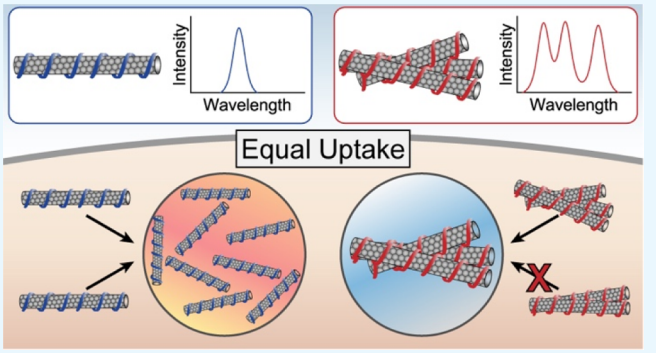

KEYWORDS: *near-infrared fluorescence, confocal Raman microscopy, nanotoxicity, nanoparticle agglomeration, carbon nanotubes*

INTRODUCTION

Bionanotechnology is an important field in biomedical research that encompasses the use of various nanoparticles and nanostructured materials for applications in drug delivery,[1] biosensing,[2] and bioimaging.[3,4] Nanoparticles are uniquely suited for biological sensing and imaging due to their nanoscale size, emergent optical,[3] electronic,[5] and magnetic properties,[6] and ability to exhibit enhanced biocompatibility upon functionalization.[7] One carbon-based nanoparticle whose fundamental properties have been highly investigated is the single-walled carbon nanotube (SWCNT). SWCNTs are desirable for use as biological sensors due to their intrinsic fluorescence which is photostable,[8] environmentally responsive,[9] and emitted at the near-infrared (NIR) wavelengths of light.[10] Additionally, SWCNTs are intriguing for use in the field of intracellular biosensing and imaging due to their one-dimensional structure and diversity of species known as chiralities.[11,12] Unprocessed SWCNTs are intrinsically hydrophobic and must first be complexed with either surfactants[13,14] or other amphiphilic molecules[15,16] to be dispersed in aqueous solutions and increase colloidal stability.[17,18] In biomedical applications, single-stranded DNA has been shown to solubilize SWCNTs *via* π-stacking and hydrophobic interactions,[19] producing DNA−SWCNT hybrid nanomaterials with substantially enhanced biocompatibility.[20] These DNA−SWCNT complexes have been incorporated into biomaterials,[21,22] introduced into biological fluids,[23,24] and immobilized in high-resolution imaging substrates[25] as biosensors to detect various physiological processes. Moreover, DNA−SWCNTs can be internalized by cells *via* active endocytosis,[26] where their optical properties can be employed to investigate specific cellular processes[27,28] and detect intracellular biomolecules.[29,30]

Despite significant recent advances within the field of bionanotechnology, there are still underlying issues regarding the physical states of the nanomaterials that must be addressed. Aggregation is often overlooked when considering how SWCNTs interact with their surroundings upon introduction to complex biological environments.[31−33] It is well established

Received: February 5, 2022
Accepted: April 8, 2022

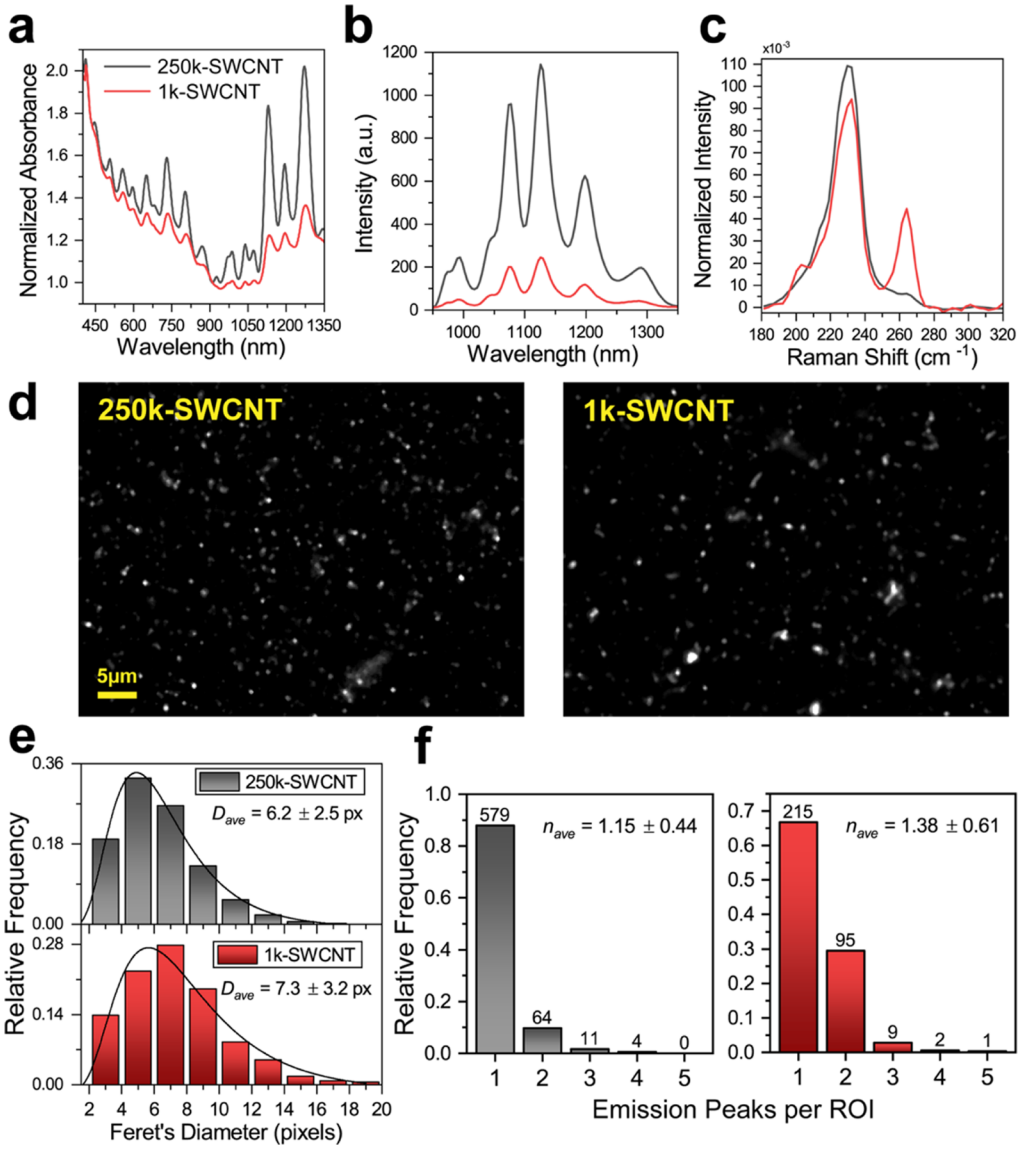

Figure 1. Optical characterization of DNA–SWCNT samples. (a) Absorbance spectra, normalized at 910 nm, (b) NIR fluorescence spectra for equal concentrations of SWCNTs (20 mg L^{-1}), and (c) normalized Raman spectra of 250k-SWCNTs and 1k-SWCNTs in solution. (d) Broadband NIR fluorescence images of the two DNA–SWCNT preparations in a spin-coated hydrogel platform. (e) Histograms of the Feret's diameter of DNA–SWCNT ROIs from NIR fluorescence images. (f) Histograms of the number of nanotube emission peaks per fluorescent ROI obtained from the two DNA–SWCNT preparations. n > 300 ROIs per sample.

that a biomolecular corona can form around DNA–SWCNTs in the presence of proteins, lipids, carbohydrates, and so forth, in cell media and biological fluids;[34−37] however, the subsequent aggregation between SWCNT–biomolecule complexes can create much larger particles than their initial, singly dispersed form.[24,37] These larger-sized aggregates can differentially interact with cells and tissues when compared to singly dispersed SWCNTs in pristine laboratory experiments,[38] and as a result, their presence can influence experimental outcomes. In the case of DNA–SWCNT biosensors, which rely on an optical response upon environmental interactions,[27,39,40] aggregation inherently alters these dynamics by reducing analyte accessibility to the SWCNT surface. Moreover, direct SWCNT aggregation can reduce or completely quench the fluorescence signal[27,41] in addition to modulating emission wavelength,[27] creating convoluted noise in a signal designed to detect specific analytes.[42]

Another issue that must be addressed concerning nanoparticle usage for biomedical sensing is the possible cytotoxic effects of the nanoparticles and if the aggregation state has any effect on the cytotoxicity. Generally, an inverse relationship between particle size and cytotoxicity has been observed for a range of nanoparticles,[43] partially explained by the increase in the surface area as particle size decreases. Consequently, cells interact much differently with small nanoparticles (<100 nm) than larger nanoscale or even micron-sized particles.[44−46] There have been many studies which have determined the effects of nanoparticle size, shape, and charge on cell–nanoparticle interactions;[46] however, aggregation will inherently alter these characteristics and has been largely ignored in the past. Previous research has shown that larger agglomerations of SWCNTs are less cytotoxic when compared to an equal weight of singly dispersed SWCNTs due to their reduced surface area-to-volume ratios.[47] It was concluded that the

https://doi.org/10.1021/acsami.2c02238
ACS Appl. Mater. Interfaces XXXX, XXX, XXX−XXX

SWCNT aggregates displayed a reduced amount of hydrophobic surfaces, when normalized by total SWCNT weight, which has been attributed to deleterious and toxic effects in cells.[47] Additionally, we have shown that intracellular trafficking processes can induce aggregation of singly dispersed DNA−SWCNTs within the lysosomes of cells.[27] In the context of translating these novel sensing and imaging technologies into clinical use, it therefore becomes important to investigate how an initially aggregated SWCNT sample is processed within various types of cells.

Here, we investigate the differential uptake, optical modulations as a result of intracellular processing, and resulting cytotoxicity of DNA−SWCNTs as a function of the aggregation state and cell type. Three cell lines were chosen, RAW 264.7 murine macrophages, HeLa human cervical cancer cells, and A549 adenocarcinomic human alveolar cells, representing a diverse range of potential interactions in addition to having application-based relevance. We define an aggregated sample as the one in which a significant proportion of the nanotubes is irreversibly bound to each other in solution due to hydrophobic interactions. We find that when dosing cells with equal concentrations of either singly dispersed or initially aggregated DNA−SWCNTs, the difference in average uptake per cell area is insignificant between samples, across all three cell lines. Interestingly, the *in vitro* fluorescence intensity of the singly dispersed DNA−SWCNT sample was significantly higher than the fluorescence intensity of the initially aggregated sample across each cell line. Moreover, the initially aggregated sample was shown to have reduced intracellular accumulation, as reported by a spectral counting approach. Finally, we observed elevated cytotoxicity in HeLa cervical cancer cells incubated with singly dispersed DNA−SWCNTs as compared to the initially aggregated sample, but insignificant differences in both RAW 264.7 macrophages and A549 lung cancer cells were observed. These results have significant implications for the rational design of novel nanosensors and imaging agents that function robustly in live cells and animals with limited toxicities.

RESULTS AND DISCUSSION

Characterization of DNA−SWCNT Suspensions. DNA-wrapped SWCNTs were prepared by probe-tip sonication and subsequent centrifugation of an aqueous mixture of single-stranded $(GT)_{15}$ oligonucleotides and HiPco SWCNTs. The sample quality, that is, the amount and degree of nanotube aggregation, was controlled during this process to obtain two distinct samples from the same starting components. A high-quality, essentially monodisperse sample and a low-quality, heterogeneously aggregated sample (hereby referred to as 250k-SWCNT and 1k-SWCNT, respectively) were created by altering the sonication and centrifugation parameters (Figure S1). Absorbance spectroscopy was used to confirm differential suspension of the two samples (Figure 1a), which exhibited clear differences in the peak-to-valley ratios in both the NIR and visible regions of the spectra. The fluorescence spectra of both samples were obtained *via* excitation with a 730 nm laser (Figure 1b). Multiple emission peaks could be observed in the NIR region; however, the integrated fluorescence intensity of 1k-SWCNTs was nearly four times lower (21.2%) than that of 250k-SWCNTs despite the same solution concentration (20 mg L^{-1}). The radial breathing mode (RBM) region of the Raman spectrum of each suspension was acquired with a 1.58 eV (785 nm) excitation (Figure 1c), revealing a clear increase in the 1k-SWCNT (10,2) peak intensity at 267 cm^{-1} relative to that of 250k-SWCNT. To summarize, the increased optical absorbance and fluorescence intensities of 250k-SWCNTs suggest a higher degree of singly dispersed nanotubes compared to that of 1k-SWCNTs.[48] Furthermore, given the 785 nm laser excitation, the intensity of the (10,2) RBM peak can be directly attributed to the degree of aggregation within a sample,[27] indicating the presence of aggregated nanotubes within the 1k-SWCNT sample.

To directly visualize the two DNA−SWCNT samples, we employed a spin-coated hydrogel platform to interrogate the NIR fluorescence with single-SWCNT resolution.[25] Briefly, a thin layer of agarose was spin-coated on a glass substrate, and the 250k-SWCNTs or 1k-SWCNTs were embedded between the second agarose layer and the first one, resulting in a single focal plane of nanotubes with preserved optical properties. Broadband NIR fluorescence (900−1600 nm) images were obtained for both samples at 100× magnification (Figure 1d). Generally, larger particles could be identified in the 1k-SWCNT sample, while the majority of fluorescent regions appeared smaller in the 250k-SWCNT fluorescent micrographs. To quantify these differences, the images were processed and a global intensity threshold was applied to obtain regions of interest (ROIs) corresponding to individual groups of fluorescent pixels. Feret's diameter, defined as the largest distance between two points in a group of pixels,[49] was calculated for each ROI and histograms were constructed (Figure 1e), revealing a higher frequency of larger-diameter ROIs present in the 1k-SWCNT sample. Due to the optical diffraction limit of our system (~500 nm) and the pixel size of our detector (~150 nm),[25] emission from a single SWCNT is blurred across a minimum of 3 × 3 pixels in NIR fluorescence images, and thus, small bundles and aggregates of SWCNTs could not be resolved from the single-nanotube population using Feret's diameter measurements. Therefore, we employed a spectral counting method to investigate the degree of aggregation for each sample.[50] Hyperspectral cubes of the spin-coated DNA−SWCNTs were acquired and again split into fluorescent ROIs. The fluorescence spectrum from each ROI was manually observed, and the number of distinct fluorescence emission peaks was quantified (Figure S2), providing a metric to spectrally resolve multiple nanotubes in diffraction-limited regions. Histograms were constructed to show the relative frequency of emission peaks per ROI (Figure 1f). Although the majority of ROIs (*i.e.*, median) from both samples contained only one fluorescence emission peak, the 1k-SWCNT population exhibited a marked increase in the amount of ROIs containing more than one emissive nanotube, suggesting elevated amounts of nanotube aggregates. We acknowledge that this method is unable to resolve the presence of multiple SWCNTs of the same chirality, that is, overlapping peaks, in addition to non-emissive nanotube species such as metallic chiralities. However, the method can differentiate aggregates which exhibit multiple peaks in the fluorescence spectrum from single CNTs which would only contain one peak. Therefore, we conclude that the clear differences between the peak per ROI distributions, Feret's diameter histograms, and characteristic optical spectra confirmed increased amounts of nanotube bundles and aggregates in the 1k-SWCNT sample relative to the singly dispersed 250k-SWCNT solution.

Intracellular Fluorescence Intensity is Cell type-Dependent. The two DNA−SWCNT samples were intro-

https://doi.org/10.1021/acsami.2c02238
ACS Appl. Mater. Interfaces XXXX, XXX, XXX−XXX

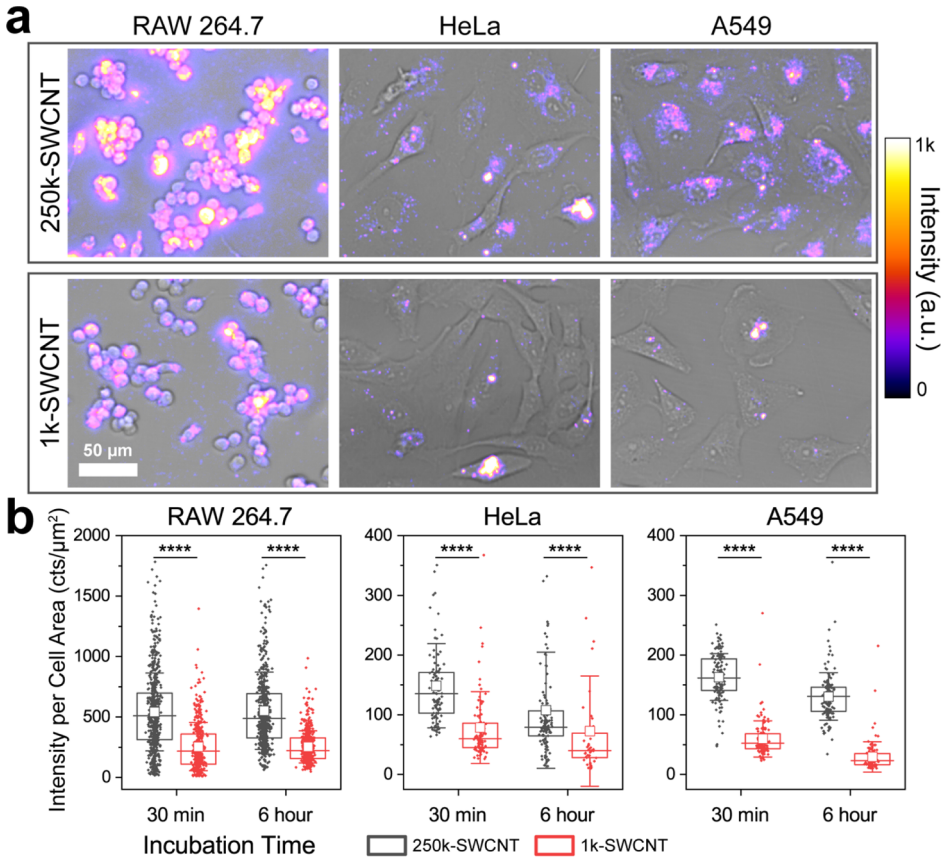

Figure 2. Cell type-dependent intracellular fluorescence of DNA–SWCNTs. (a) Transmitted light images overlaid with broadband NIR fluorescence micrographs of RAW 264.7, HeLa, or A549 cells dosed with 250k- or 1k-SWCNTs for 30 min and incubated for an additional 6 h. (b) Broadband fluorescence intensity per total cell area from individual cells as a function of the DNA–SWCNT sample and incubation time for each cell line. Minimum of $n \geq 96$ cells per condition were used. Boxes represent 25–75% of the data, white squares represent means, horizontal lines represent medians, and whiskers represent mean ± s.d. One-way ANOVA with Tukey posthoc analysis was performed (****$p < 1 \times 10^{-4}$).

duced into live mammalian cells in culture to investigate how the sample quality influences their interactions with biological systems. We chose three distinct cell types to represent a range of potential interactions which could be encountered with *in vitro* cell lines: RAW 264.7 murine macrophages; HeLa human cervical adenocarcinoma epithelial cells; and A549 human lung carcinoma epithelial cells. The interactions between macrophages and nanoparticles, especially biologically aggregated and protein-adsorbed nanoparticles, are important to investigate because macrophages are among the first cells to process nanoparticles in systemic circulation.[51] HeLa cells were investigated due to their widespread usage for *in vitro* modeling of nanoparticle uptake and cytotoxicity.[52−54] Finally, A549 lung cancer cells were chosen due to an increasing interest in delivering drug-loaded nanoparticles directly into the lungs to treat disease, creating a relevance to investigate how lung cells interact with aggregated nanoparticles.[55] Each cell type was dosed with 1 mg L^{-1} 250k-SWCNT or 1k-SWCNT for 30 min, rinsed, and allowed to incubate for an additional 30 min or 6 h to promote cell uptake and localization of the DNA–SWCNTs in the early endosomes or late endosomes/lysosomes, respectively,[27] after which broadband NIR fluorescence images were acquired from the live cells. Figure 2a shows fluorescence images from each condition at the 6 h time point. In general, cells dosed with the 250k-SWCNTs exhibited increased intracellular fluorescence intensities compared to those dosed with the 1k-SWCNTs, while RAW 264.7 cell fluorescence appeared to be the brightest among the three cell lines. To quantify these differences, we first segmented the cells from each image into individual ROIs using the transmitted light images obtained in parallel (Figure S3). The integrated NIR fluorescence intensity was then calculated for each cell ROI and divided by the total cell area, producing intensity measurements that normalized for the substantial differences in cell type sizes. Box plots were constructed from all single-cell measurements to compare each condition (Figure 2b). Clear differences in the cell intensity distributions were identified between cells dosed with 250k-SWCNTs and 1k-SWCNTs, the former of which were significantly more intense, regardless of cell type and incubation time. Additionally, fluorescence from RAW 264.7 cells was significantly more intense than that from the other cell lines (Figure S4), an expected result which is directly related to the phagocytotic nature of macrophages.

Two potential factors could explain why cells dosed with 1k-SWCNTS were substantially less intense than those dosed with 250k-SWCNTs: (1) DNA–SWCNT uptake is higher for monodisperse nanotubes and therefore the fluorescence intensity is also higher or (2) uptake is the same and the fluorescence of internalized nanotubes is decreased by the presence of bundles and aggregates. To account for the intrinsic fluorescence intensity differences observed between the two DNA–SWCNT preparations (Figure 1c), we determined a quenching coefficient from a series of control experiments (Figure S5). Next, we applied this coefficient to

https://doi.org/10.1021/acsami.2c02238
ACS Appl. Mater. Interfaces XXXX, XXX, XXX−XXX

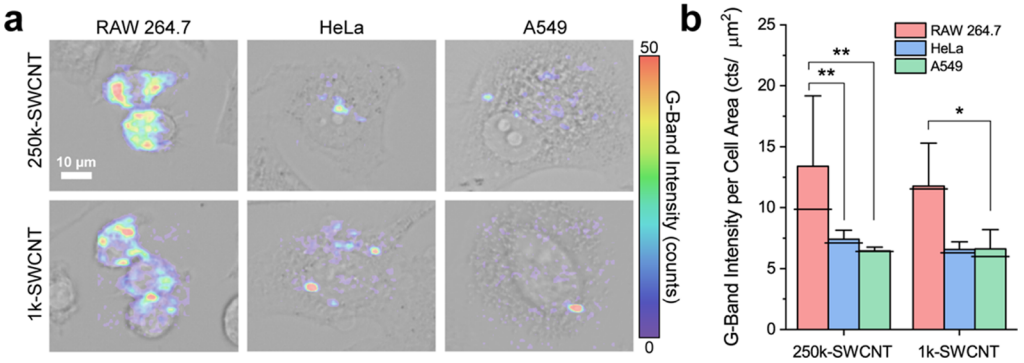

Figure 3. DNA–SWCNT uptake *via* confocal Raman microscopy. (a) Transmitted light images of RAW 264.7, HeLa, or A549 cells overlaid with G-band intensity maps of intracellular 250k-SWCNTs and 1k-SWCNTs after 6 h. (b) Bar graph of intracellular G-band intensity per cell area for each cell line. Bars represent the average, lines represent the median, and whiskers represent mean ± s.d. for each condition ($n \geq 4$ cells per condition). One-way ANOVA with Tukey posthoc analysis was performed between cell lines dosed with the same DNA–SWCNT sample (**$p < 0.01$ and *$p < 0.05$).

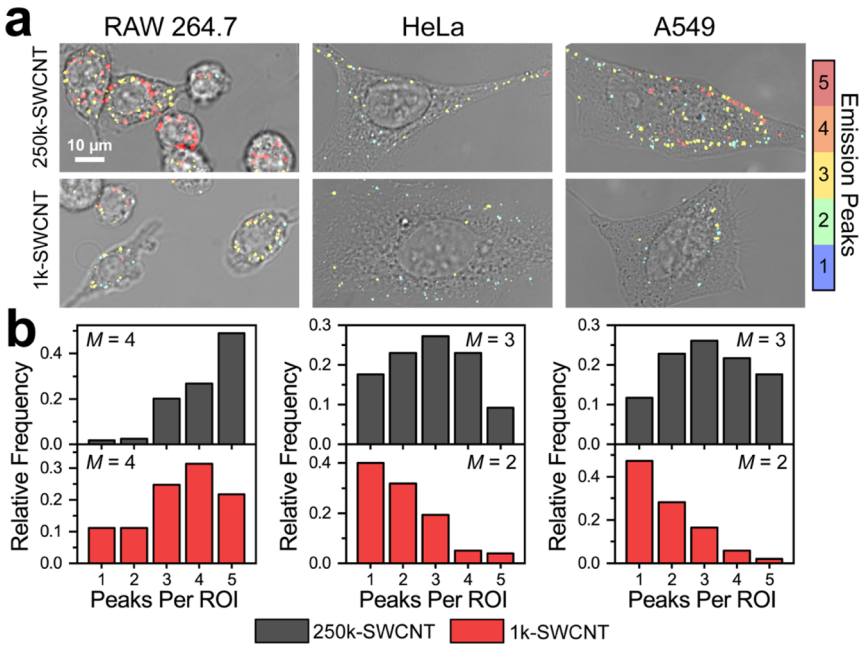

Figure 4. Spectral counting quantifies endosomal nanotube loading. (a) Transmitted light images overlaid with ROI maps and false-colored by the number of emission peaks detected for cells dosed with 250k-SWCNTs (top) or 1k-SWCNTs (bottom). (b) Histograms of the SWCNT emission peaks per ROI for all cells ($n > 150$ ROIs per condition) with median values (M) indicated.

the intracellular 1k-SWCNT data to account for these intrinsic differences and compared the corrected intensity values with those from the 250k-SWCNT-dosed cells (Figure S6). Interestingly, the correction factor resulted in near-identical values for the 250k-SWCNT- and 1k-SWCNT-dosed cells at the 30 min time point, suggesting that the latter case could be viable. The trend was relatively similar at the 6 h time point (Figure S6b).

Cell Uptake is Independent of DNA–SWCNT Dispersion Quality. We employed confocal Raman microscopy to quantitatively probe the cell type-dependent uptake of each DNA–SWCNT preparation. Cells were again dosed with 1 mg L^{-1} of 250k-SWCNTs or 1k-SWCNTs for 30 min, washed, and placed into fresh media for an additional 6 h, the time at which the samples were fixed and prepared for confocal Raman microscopy. Hyperspectral Raman images were acquired from individual cells at 100× magnification to investigate the G-band (Figure S7), a Raman feature of SWCNTs which linearly scales with SWCNT concentration.[56,57] G-band intensity images were constructed and overlaid with transmitted light images for cells in each condition (Figure 3a), and the uptake was quantified as the integrated G-band intensity per cell area (Figure 3b). The SWCNT uptake was highest into RAW 264.7 macrophages, which internalized at least 78% more DNA–SWCNTs than HeLa and A549, regardless of the dosed DNA–SWCNT sample. This finding confirmed that higher nanotube uptake contributed to the increased fluorescence intensities seen previously in the macrophages relative to HeLa and A549 cells. In contrast, the difference in uptake between the 250k-SWCNTs and the 1k-SWCNTs was insignificant in any particular cell line ($p > 0.05$ according to two-sample two-tailed student t-test for each cell line), further supporting the hypothesis that variations in intrinsic brightness of the samples (see Figure 1b) contributed to the significantly different fluorescence intensity values.

https://doi.org/10.1021/acsami.2c02238
ACS Appl. Mater. Interfaces XXXX, XXX, XXX–XXX

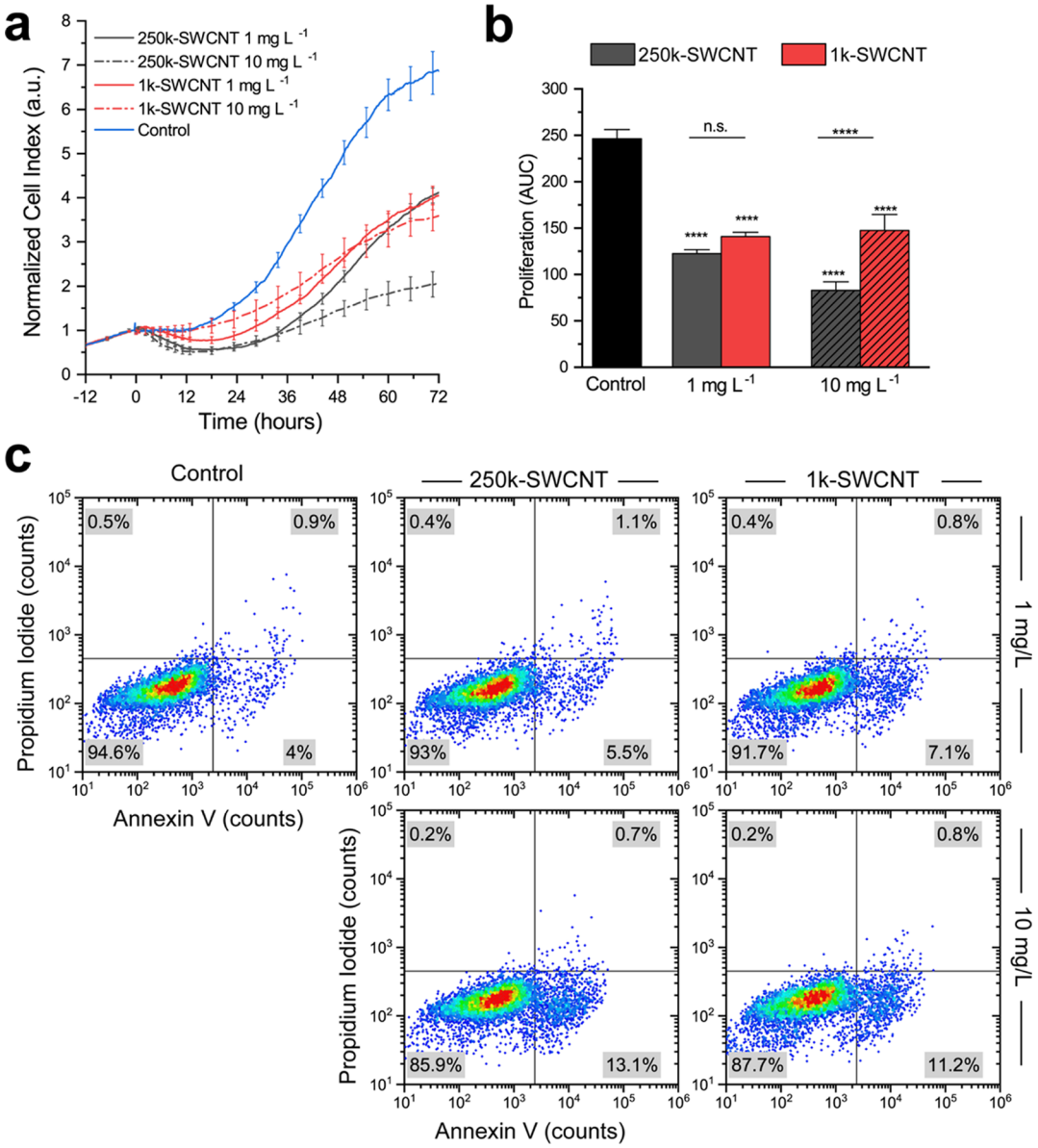

Figure 5. Cell proliferation and viability to identify adverse responses. (a) Real-time monitoring of HeLa proliferation after addition of indicated DNA−SWCNTs *via* xCELLigence impedance measurements. The line represents the mean cell index (n = 4), and error bars represent the mean ± s.d. Data were normalized to the final measurement before nanotube exposure. For clarity, error bars are shown on 1 out of every 20 data points. (b) Bar graph representing total proliferation using the mean integrated AUC from the data shown in (a). One-way ANOVA with Tukey posthoc analysis was performed (****$p < 1 \times 10^{-4}$). Stars directly above the bars represent significance *vs* control. (c) Scatter plots depicting apoptosis data for control cells (left) and cells dosed with 1 or 10 mg-L^{-1} of either 250k-SWCNTs (center) or 1k-SWCNTs (right). Viable, apoptotic, and necrotic cells are found in the bottom left, bottom right, and top right quadrants, respectively.

Dispersion Heterogeneity Reduces Intracellular Nanotube Accumulation. Next, we sought to investigate how the intracellular processing of DNA−SWCNTs can vary depending on the dispersion quality. As a quantitative measure of this processing, the endosomal loading of DNA−SWCNTs was interrogated using the same hyperspectral counting approach previously described within single intracellular ROIs of the three cell lines.[50] Hyperspectral cubes were acquired at 100× magnification for each cell type following a 30 min pulse of 250k-SWCNTs or 1k-SWCNTs and an additional 30 min of incubation in fresh media. Subsequent spectral counting analysis and spectral image overlays revealed that the number of emission peaks ranged from one to five for all conditions (Figure 4a). For ROI populations from both DNA−SWCNT dispersions (Figure 4b), RAW 264.7 cells were observed to contain the highest total fraction of ROIs with ≥four emission peaks relative to the ROI distributions from HeLa and A549 cells. Nanotube dispersion quality was also a major contributing factor to the subcellular localization of DNA−SWCNTs. Regardless of the cell line, intracellular ROIs were more likely to contain more emissive nanotubes when dosed with the 250k-SWCNTs versus the lesser-quality 1k-SWCNTs. To explain this anomaly, we hypothesized that despite equal total nanotube uptake, cells were more likely to intracellularly combine the cargo from internalized vesicles when single SWCNTs or small quantities were encapsulated. In contrast, the intracellular ROI peak distribution of 1k-SWCNTs in HeLa and A549 more closely resembled that of

https://doi.org/10.1021/acsami.2c02238
ACS Appl. Mater. Interfaces XXXX, XXX, XXX−XXX

the starting sample shown in Figure 1f compared to the 250k-SWCNT distributions. These results could indicate the downregulation of a particular endosomal maturation pathway[58] if the initial load of nanotubes is above a certain threshold. In this scenario, the subcellular localization and accumulation, that is, processing into regions of high local SWCNT density, could be controlled by modulating the initial DNA−SWCNT dispersion quality.

Proliferation and Cytotoxicity. To quantify potential deleterious effects on cell health as a function of dispersion quality, we utilized two diverse methods to assess the response of each cell line to a constant dose of DNA−SWCNTs. First, real-time cell proliferation was monitored using an xCELLigence system, which measures electrical impedance across interdigitated micro-electrodes embedded in the bottom of specialized tissue culture E-plates.[59] The impedance measurement, represented as a cell index value, can then be directly correlated to various cellular characteristics including cell number, viability, and morphology.[59] Cells were seeded in the tissue culture E-plates and incubated for 24 h, after which a dose of 250k-SWCNTs or 1k-SWCNTs was introduced into the culture media and allowed to incubate for the remainder of the experiment. To compare relative proliferations between the different conditions, the cell index was normalized to the final measurement taken before nanotube dosing (time 0). HeLa cells exhibited a clear response to the addition of both types of DNA−SWCNTs and at standard (1 mg L^{-1}) and elevated (10 mg L^{-1}) concentrations relative to a no SWCNT control (Figure 5a). Interestingly, RAW 264.7 and A549 did not show the same trend (Figures S8 and S9) and in certain cases responded to the dose by increasing the rate of proliferation relative to control cells. We calculated the average area under the curve (AUC) as a quantitative measure to compare the total growth following nanotube exposure (Figure 5b). The proliferation relative to the control was significantly reduced in the continuous presence of DNA−SWCNTs; however, 250k-SWCNTs appeared to have a greater negative impact that scaled with dosing concentration when compared to the 1k-SWCNTs. Next, an apoptosis−necrosis assay was performed on HeLa cells using the same incubation conditions from the proliferation experiment to directly assess the potential for cytotoxicity. When incubating the HeLa cells with 1 mg L^{-1} of SWCNTs continuously for 24 h, a slight increase in the apoptotic cell population was apparent from both of the nanotube dispersions relative to the control cells (Figure 5c). At 10 mg/L^{-1}, a shift in the cell population was evident for both samples of DNA−SWCNTs (Figure 5c), inducing over 10% cells to become apoptotic over a 24 h period due to nanotube exposure.

CONCLUSIONS

The goal of this study was to systematically investigate nanoscale aggregation as a fundamental material property and characterize the resulting cellular interactions. Two DNA−SWCNT samples were differentially fabricated from the same starting material to produce a monodisperse sample and a low-quality dispersion with defined levels of aggregation. We found that, when equally dosed, the rate of uptake was independent of the starting sample quality in any given cell line. The number of nanotubes within individual subcellular regions was quantified upon internalization using a hyperspectral counting method. Higher quantities of nanotubes were consistently found in subcellular regions when dosed with a monodisperse sample, while the intracellular distribution of aggregates appeared to match the stock sample population. This sample dependence could indicate that single SWCNTs can be selectively accumulated in single vesicles upon internalization, and thus, the degree of aggregation could influence certain intracellular pathways. Cell proliferation and viability were also found to be lower in cells dosed with monodisperse nanotubes, further indicating that the aggregation state modulates internalization and processing mechanisms. Therefore, the effects of aggregation must be acknowledged when characterizing nanomaterials in biological settings.

MATERIALS AND METHODS

DNA−SWCNT Sample Preparation. Raw SWCNTs produced by the HiPco process (Nanointegris) were used throughout this study. For each dispersion, 2 mg of $(GT)_{15}$ oligonucleotide (Integrated DNA Technologies) was added to 1 mg of raw nanotubes in 1 mL of 0.1 M NaCl (Sigma-Aldrich) in deionized water. The singly dispersed sample (250k-SWCNT) was ultrasonicated using a 1/8″ tapered microtip for 30 min at 40% amplitude (Sonics Vibracell VCX-130; Sonics and Materials). The resulting suspension was ultracentrifuged (Sorvall Discovery M120 SE) for 30 min at 250,000*g*, and the top ∼80% of the supernatant was collected. The initially aggregated sample (1k-SWCNT) was ultrasonicated using a 1/8″ tapered microtip for 5 min at 40% amplitude (Sonics Vibracell VCX-130; Sonics and Materials). The resulting suspension was benchtop-centrifuged (Eppendorf Centrifuge 5430 R) for 5 min at 1000*g*, and the top ∼25% of the supernatant was collected. Concentrations were determined using a UV/vis/NIR spectrophotometer (JASCO, Tokyo, Japan) and an extinction coefficient of A_{910} = 0.02554 L mg^{-1} cm^{-1}.[60]

NIR Fluorescence Microscopy. A NIR hyperspectral fluorescence microscope, comparable to a previously detailed system,[60] was used to obtain all hyperspectral fluorescence data. In short, a 730 nm excitation laser source was reflected on the sample stage of an Olympus IX-73 inverted microscope equipped with either a UApo N 100×/1.49 oil immersion IR objective (Olympus, USA) or a LCPlan N, 20×/0.45 IR objective (Olympus, U.S.A.), as indicated in the figure captions. The resulting fluorescence emission was passed through a volume Bragg grating and collected with a 2D InGaAs array detector (Photon Etc., Montreal, Canada) to generate spectral image stacks. Live-cell samples were mounted on a stage top incubator unit (Okolab) to maintain 37 °C and 5% CO_2 culture conditions throughout the imaging procedure. All hyperspectral cubes, broadband fluorescence images, and transmitted light images were corrected and processed in Matlab.

Diffraction-Limited Fluorescence Imaging of DNA−SWCNTs. DNA−SWCNT samples were prepared for direct 100× NIR fluorescence imaging using a spin coating technique to embed a single focal plane of SWCNTs between thin hydrogel layers.[25] Briefly, a thin film of 2% agarose was deposited on a glass coverslip by spin coating 450 μL at 1400 rpm for 30 s. The first layer was allowed to solidify before 200 μL of 5 mg/L 250k-SWCNTs or 1k-SWCNTs was subsequently spin-coated on the agarose surface at 1000 rpm for 30 s. A final agarose layer was cast on top of the spin-coated films and allowed to gel for at least 5 min. The hydrogel samples were mounted on a NIR hyperspectral fluorescence microscope with excess DI water during fluorescence data acquisition.

Cell Culture. RAW 264.7 TIB-71, HeLa CCL-2, and A549 CCL-185 cell lines (ATCC, Manassas, VA, USA) were cultured under standard incubation conditions at 37 °C and 5% CO_2. D-10 cell culture medium containing sterile filtered high-glucose DMEM with 10% heat-inactivated FBS, 2.5% HEPES, 1% L-glutamine, 1% penicillin/streptomycin, and 0.2% amphotericin B (all acquired from Gibco) was used for all cell lines.

***In Vitro* Sample Preparation for Optical Microscopy.** For all *in vitro* 20× NIR fluorescence imaging experiments, cells were seeded into 24-well tissue culture plates (CELLTREAT) to concentrations of 5.26 × 10^4 (RAW) or 2.11 × 10^4 cells/cm^2 (HeLa/A549) and

https://doi.org/10.1021/acsami.2c02238
ACS Appl. Mater. Interfaces XXXX, XXX, XXX−XXX

allowed to culture overnight. To dose the cells, the medium was removed from each culture dish, replaced with 1 mg/L of either 250k-SWCNTs or 1k-SWCNTs diluted in medium, and incubated for 30 min to allow internalization into the cells. The SWCNT-containing medium was subsequently removed, and the cells were rinsed twice with sterile phosphate buffered saline (PBS, Gibco) before fresh medium was replenished. All time points were defined with respect to this step, that is, 30 min or 6 h after the SWCNT medium was removed from the cells. For all 100× NIR fluorescence imaging and 20× confocal Raman microscopy experiments, the cells were seeded into 35 mm glass-bottom microwell dishes (MatTek) to the same concentrations as previously listed and allowed to culture overnight. The same SWCNT dosing procedure was followed; however, cells were fixed at each time point. Fixation was performed with 4% paraformaldehyde in PBS for 15 min, after which the cells were rinsed three times and covered with PBS to retain an aqueous environment during imaging.

Confocal Raman Microscopy. All Raman data were acquired using an inverted WiTec Alpha300 R confocal Raman microscope (WiTec, Germany) equipped with an Olympus LCPlan N, 20×/0.45 IR objective, a 785 nm laser (35 mW output measured at the sample), and a UHTS 300 spectrograph (300 lines/mm grating) coupled with an Andor DR32400 CCD detector (−61 °C, 1650 × 200 pixels). Small cellular areas were scanned, and spectra were obtained in 1 × 1 μm intervals using a 0.8 s integration time per spectrum to construct hyperspectral images of individual cells. Global background subtraction and cosmic ray removal were performed in each scan using Witec Project 5.2 software. Hyperspectral data were extracted and processed using custom codes written with Matlab software.

Hyperspectral Counting. We utilized hyperspectral counting,[50] a recently developed quantitative technique, to estimate the number of SWCNTs contained in diffraction-limited ROIs. Briefly, hyperspectral images were acquired at 100× magnification, initially processed to correct for background intensities, and split into individual ROIs corresponding to localized fluorescence from one or more nanotubes. ROIs were determined manually in FIJI for all DNA−SWCNT characterization data, while a previously developed segmentation pipeline[27] was globally applied to all cell data to identify ROIs based on pixel intensities and morphological structures. Analysis was then carried out individually on each ROI, from which the average fluorescence spectrum was extracted, labeled, and compiled into one of two data sets corresponding to either direct SWCNT imaging or intracellular fluorescence data. Once all data were pooled appropriately, each spectrum was manually viewed to assess the number of identifiable emission peaks from each ROI. Additionally, a custom Matlab application was designed to facilitate the blind analysis of >1000 intracellular ROI spectra acquired for all conditions.

Label-Free Cell Proliferation and Adherence Monitoring. Proliferation and adherence were measured using an xCELLigence real-time cell analysis (RTCA) instrument (Agilent). To measure the baseline impedance of the wells, 140 μL of cell media was added to each of the RTCA E-plate wells. Next, 50 μL of cells diluted in medium was added to each well to reach final concentrations of 20,000 cells/well (RAW), 2500 cells/well (HeLa), or 4000 cells/well (A549). The cells were allowed to adhere to the plates for 30 min in a cell culture hood to reduce convection currents, allowing for an evenly distributed initial seeding of cells over the electrodes. After 30 min, the E-plates were placed into the xCELLigence instrument, and data acquisition occurred every 15 min. After 24 h, each plate was spiked with 10 μL of either 250k-SWCNTs or 1k-SWCNTs diluted in media to reach final concentrations of 1 or 10 mg/L. Data acquisition occurred every 1 min for 60 min, then every 5 min for 12 h, and finally every 15 min for the remainder of the experiment. Data were normalized to the last measured data point before SWCNT addition, and n = 4 wells were used for each experimental data set.

Cell Viability Assay Image Cytometry Assay. Cells were plated on 35 mm glass-bottom microwell dishes (MatTek) and were allowed to culture overnight. Initial plating cell concentrations were 5.26 × 10^4 cells/cm^2 (RAW), 1.59 × 10^4 cells/cm^2 (HeLa), and 2.11 × 10^4 cells/cm^2 (A549). The following day, the medium was replaced with 1 mg/L of either singly dispersed or initially aggregated $(GT)_{15}$-SWCNTs diluted in media and incubated for 24 h. After 24 h, the cells were collected from the dishes and stained with Annexin V and propidium iodide (Dead Cell Apoptosis Kit V13242, Invitrogen) following the manufacturer's protocol. Fluorescence images of the stained cells were acquired by using a Cellometer Vision CBA image cytometer (Nexcelom Bioscience), and images were analyzed by using ImageJ and custom Matlab codes. For each cell condition, a control dish was plated without SWCNT addition to create the gates on the Annexin V and propidium iodide axes of the histograms.

Statistical Analysis. OriginPro 2018 was used to perform all statistical analyses. All data either met assumptions of the statistical tests performed (*i.e.*, normality, equal variances, *etc.*) or were transformed to meet assumptions before statistical analysis was carried out. Statistical significance was analyzed using two-sample two-tailed Student t-test or one-way ANOVA where appropriate. Testing of multiple hypotheses was accounted for by performing one-way ANOVA with Tukey's posthoc test. Specific information about statistical analyses can be found in figure legends.

■ ASSOCIATED CONTENT

Supporting Information

The Supporting Information is available free of charge at https://pubs.acs.org/doi/10.1021/acsami.2c02238.

Schematic of DNA−SWCNT sample preparation, spectral counting emission peak examples, single-cell ROI analyses, comparison of intracellular fluorescence between cell lines, stock sample fluorescence intensities, intensity-corrected intracellular fluorescence, DNA−SWCNT Raman spectra, and additional proliferation and viability results for RAW 264.7 and A549 cells (PDF)

■ AUTHOR INFORMATION

Corresponding Author

Daniel Roxbury − *Department of Chemical Engineering, University of Rhode Island, Kingston, Rhode Island 02881, United States;* orcid.org/0000-0003-2812-3523; Email: roxbury@uri.edu

Authors

Mitchell Gravely − *Department of Chemical Engineering, University of Rhode Island, Kingston, Rhode Island 02881, United States;* orcid.org/0000-0001-7938-6054

Aidan Kindopp − *Department of Chemical Engineering, University of Rhode Island, Kingston, Rhode Island 02881, United States*

Lauren Hubert − *Department of Chemical Engineering, University of Rhode Island, Kingston, Rhode Island 02881, United States*

Matthew Card − *Department of Chemical Engineering, University of Rhode Island, Kingston, Rhode Island 02881, United States;* orcid.org/0000-0002-0471-0961

Aceer Nadeem − *Department of Chemical Engineering, University of Rhode Island, Kingston, Rhode Island 02881, United States*

Christopher Miller − *Department of Chemical Engineering, University of Rhode Island, Kingston, Rhode Island 02881, United States*

Complete contact information is available at: https://pubs.acs.org/10.1021/acsami.2c02238

Notes

The authors declare no competing financial interest.

■ ACKNOWLEDGMENTS

This work was supported by the National Science Foundation CAREER Award #1844536 and the University of Rhode Island College of Engineering. The confocal Raman data were acquired at the RI Consortium for Nanoscience and Nanotechnology, a URI College of Engineering core facility partially funded by the National Science Foundation EPSCoR, Cooperative Agreement #OIA-1655221.

■ REFERENCES

(1) Wilczewska, A. Z.; Niemirowicz, K.; Markiewicz, K. H.; Car, H. Nanoparticles as Drug Delivery Systems. *Pharmacol. Rep.* **2012**, *64*, 1020−1037.
(2) Luo, X.; Morrin, A.; Killard, A. J.; Smyth, M. R. Application of Nanoparticles in Electrochemical Sensors and Biosensors. *Electroynalysis* **2006**, *18*, 319−326.
(3) Sharma, P.; Brown, S.; Walter, G.; Santra, S.; Moudgil, B. Nanoparticles for Bioimaging. *Adv. Colloid Interface Sci.* **2006**, *123*−*126*, 471−485.
(4) Liu, Z.; Yang, K.; Lee, S.-T. Single-Walled Carbon Nanotubes in Biomedical Imaging. *J. Mater. Chem.* **2011**, *21*, 586−598.
(5) Zhou, Y.; Hu, J.; Dang, B.; He, J. Effect of Different Nanoparticles on Tuning Electrical Properties of Polypropylene Nanocomposites. *IEEE Trans. Dielectr. Electr. Insul.* **2017**, *24*, 1380−1389.
(6) Kolhatkar, A.; Jamison, A.; Litvinov, D.; Willson, R.; Lee, T. Tuning the Magnetic Properties of Nanoparticles. *Int. J. Mol. Sci.* **2013**, *14*, 15977−16009.
(7) Fratila, R. M.; Mitchell, S. G.; del Pino, P.; Grazu, V.; de la Fuente, J. M. Strategies for the Biofunctionalization of Gold and Iron Oxide Nanoparticles. *Langmuir* **2014**, *30*, 15057−15071.
(8) Boghossian, A. A.; Zhang, J.; Barone, P. W.; Reuel, N. F.; Kim, J.-H.; Heller, D. A.; Ahn, J.-H.; Hilmer, A. J.; Rwei, A.; Arkalgud, J. R.; Zhang, C. T.; Strano, M. S. Near-Infrared Fluorescent Sensors Based on Single-Walled Carbon Nanotubes for Life Sciences Applications. *ChemSusChem* **2011**, *4*, 848.
(9) Heller, D. A.; Pratt, G. W.; Zhang, J.; Nair, N.; Hansborough, A. J.; Boghossian, A. A.; Reuel, N. F.; Barone, P. W.; Strano, M. S. Peptide Secondary Structure Modulates Single-Walled Carbon Nanotube Fluorescence as a Chaperone Sensor for Nitroaromatics. *Proc. Natl. Acad. Sci. U.S.A.* **2011**, *108*, 8544−8549.
(10) Lefebvre, J.; Homma, Y.; Finnie, P. Bright Band Gap Photoluminescence from Unprocessed Single-Walled Carbon Nanotubes. *Phys. Rev. Lett.* **2003**, *90*, 217401.
(11) Bachilo, S. M.; Strano, M. S.; Kittrell, C.; Hauge, R. H.; Smalley, R. E.; Weisman, R. B. Structure-Assigned Optical Spectra of Single-Walled Carbon Nanotubes. *Science* **2002**, *298*, 2361−2366.
(12) Heller, D. A.; Baik, S.; Eurell, T. E.; Strano, M. S. Single-Walled Carbon Nanotube Spectroscopy in Live Cells: Towards Long-Term Labels and Optical Sensors. *Adv. Mater.* **2005**, *17*, 2793−2799.
(13) Vaisman, L.; Wagner, H. D.; Marom, G. The Role of Surfactants in Dispersion of Carbon Nanotubes. *Adv. Colloid Interface Sci.* **2006**, *128*−*130*, 37−46.
(14) Zhang, C.; Wang, P.; Barnes, B.; Fortner, J.; Wang, Y. Cleanly Removable Surfactant for Carbon Nanotubes. *Chem. Mater.* **2021**, *33*, 4551−4557.
(15) Arnold, M. S.; Guler, M. O.; Hersam, M. C.; Stupp, S. I. Encapsulation of Carbon Nanotubes by Self-Assembling Peptide Amphiphiles. *Langmuir* **2005**, *21*, 4705−4709.
(16) Ohta, T.; Hashida, Y.; Yamashita, F.; Hashida, M. Development of Novel Drug and Gene Delivery Carriers Composed of Single-Walled Carbon Nanotubes and Designed Peptides with PEGylation. *J. Pharm. Sci.* **2016**, *105*, 2815−2824.
(17) Chaudhary, H.; Fernandes, R. M. F.; Gowda, V.; Claessens, M. M. A. E.; Furó, I.; Lendel, C. Intrinsically Disordered Protein as Carbon Nanotube Dispersant: How Dynamic Interactions Lead to Excellent Colloidal Stability. *J. Colloid Interface Sci.* **2019**, *556*, 172−179.
(18) Douroumis, D.; Fatouros, D. G.; Bouropoulos, N.; Papagelis, K.; Tasis, D. Colloidal Stability of Carbon Nanotubes in an Aqueous Dispersion of Phospholipid. *Int. J. Nanomed.* **2007**, *2*, 761.
(19) Zheng, M.; Jagota, A.; Semke, E. D.; Diner, B. A.; McLean, R. S.; Lustig, S. R.; Richardson, R. E.; Tassi, N. G. DNA-Assisted Dispersion and Separation of Carbon Nanotubes. *Nat. Mater.* **2003**, *2*, 338−342.
(20) Gao, Z.; Varela, J. A.; Groc, L.; Lounis, B.; Cognet, L. Toward the Suppression of Cellular Toxicity from Single-Walled Carbon Nanotubes. *Biomater. Sci.* **2016**, *4*, 230−244.
(21) Safaee, M. M.; Gravely, M.; Roxbury, D. A Wearable Optical Microfibrous Biomaterial with Encapsulated Nanosensors Enables Wireless Monitoring of Oxidative Stress. *Adv. Funct. Mater.* **2021**, *31*, 2006254.
(22) Madani, S. Z. M.; Safaee, M. M.; Gravely, M.; Silva, C.; Kennedy, S.; Bothun, G. D.; Roxbury, D. Carbon Nanotube−Liposome Complexes in Hydrogels for Controlled Drug Delivery via Near-Infrared Laser Stimulation. *ACS Appl. Nano Mater.* **2020**, *4*, 331−342.
(23) Pinals, R. L.; Yang, D.; Lui, A.; Cao, W.; Landry, M. P. Corona Exchange Dynamics on Carbon Nanotubes by Multiplexed Fluorescence Monitoring. *J. Am. Chem. Soc.* **2019**, *142*, 1254−1264.
(24) Pinals, R. L.; Yang, D.; Rosenberg, D. J.; Chaudhary, T.; Crothers, A. R.; Iavarone, A. T.; Hammel, M.; Landry, M. P. Quantitative Protein Corona Composition and Dynamics on Carbon Nanotubes in Biological Environments. *Angew. Chem.* **2020**, *132*, 23876−23885.
(25) Card, M.; Gravely, M.; Madani, S. Z. M.; Roxbury, D. A Spin-Coated Hydrogel Platform Enables Accurate Investigation of Immobilized Individual Single-Walled Carbon Nanotubes. *ACS Appl. Mater. Interfaces* **2021**, *13*, 31986−31995.
(26) Bhattacharya, S.; Roxbury, D.; Gong, X.; Mukhopadhyay, D.; Jagota, A. DNA Conjugated SWCNTs Enter Endothelial Cells via Rac1 Mediated Macropinocytosis. *Nano Lett.* **2012**, *12*, 1826−1830.
(27) Gravely, M.; Roxbury, D. Multispectral Fingerprinting Resolves Dynamics of Nanomaterial Trafficking in Primary Endothelial Cells. *ACS Nano* **2021**, *15*, 12388−12404.
(28) Kam, N. W. S.; Liu, Z.; Dai, H. Carbon Nanotubes as Intracellular Transporters for Proteins and DNA: An Investigation of the Uptake Mechanism and Pathway. *Angew. Chem., Int. Ed.* **2006**, *45*, 577−581.
(29) Jena, P. V.; Roxbury, D.; Galassi, T. V.; Akkari, L.; Horoszko, C. P.; Iaea, D. B.; Budhathoki-Uprety, J.; Pipalia, N.; Haka, A. S.; Harvey, J. D.; Mittal, J.; Maxfield, F. R.; Joyce, J. A.; Heller, D. A. A Carbon Nanotube Optical Reporter Maps Endolysosomal Lipid Flux. *ACS Nano* **2017**, *11*, 10689−10703.
(30) Galassi, T. V.; Jena, P. V.; Shah, J.; Ao, G.; Molitor, E.; Bram, Y.; Frankel, A.; Park, J.; Jessurun, J.; Ory, D. S.; Haimovitz-Friedman, A.; Roxbury, D.; Mittal, J.; Zheng, M.; Schwartz, R. E.; Heller, D. A. An Optical Nanoreporter of Endolysosomal Lipid Accumulation Reveals Enduring Effects of Diet on Hepatic Macrophages in vivo. *Sci. Transl. Med.* **2018**, *10*, 461.
(31) Fenoglio, I.; Fubini, B.; Ghibaudi, E. M.; Turci, F. Multiple Aspects of the Interaction of Biomacromolecules with Inorganic Surfaces. *Adv. Drug Delivery Rev.* **2011**, *63*, 1186−1209.
(32) Soddu, L.; Trinh, D. N.; Dunne, E.; Kenny, D.; Bernardini, G.; Kokalari, I.; Marucco, A.; Monopoli, M. P.; Fenoglio, I. Identification of Physicochemical Properties that Modulate Nanoparticle Aggregation in Blood. *Beilstein J. Nanotechnol.* **2020**, *11*, 550−567.
(33) Li, S.-D.; Huang, L. Pharmacokinetics and Biodistribution of Nanoparticles. *Mol. Pharm.* **2008**, *5*, 496−504.
(34) Lundqvist, M.; Stigler, J.; Cedervall, T.; Berggård, T.; Flanagan, M. B.; Lynch, I.; Elia, G.; Dawson, K. The Evolution of the Protein Corona around Nanoparticles: A Test Study. *ACS Nano* **2011**, *5*, 7503−7509.
(35) Ke, P. C.; Lin, S.; Parak, W. J.; Davis, T. P.; Caruso, F. A Decade of the Protein Corona. *ACS Nano* **2017**, *11*, 11773−11776.

https://doi.org/10.1021/acsami.2c02238
ACS Appl. Mater. Interfaces XXXX, XXX, XXX−XXX

(36) Shannahan, J. H.; Brown, J. M.; Chen, R.; Ke, P. C.; Lai, X.; Mitra, S.; Witzmann, F. A. Comparison of Nanotube−Protein Corona Composition in Cell Culture Media. *Small* **2013**, *9*, 2171−2181.
(37) Ge, C.; Tian, J.; Zhao, Y.; Chen, C.; Zhou, R.; Chai, Z. Towards Understanding of Nanoparticle−Protein Corona. *Arch. Toxicol.* **2015**, *89*, 519−539.
(38) Jiang, W.; Kim, B. Y. S.; Rutka, J. T.; Chan, W. C. W. Nanoparticle-Mediated Cellular Response is Size-Dependent. *Nat. Nanotechnol.* **2008**, *3*, 145−150.
(39) Yum, K.; Ahn, J.-H.; McNicholas, T. P.; Barone, P. W.; Mu, B.; Kim, J.-H.; Jain, R. M.; Strano, M. S. Boronic Acid Library for Selective, Reversible Near-Infrared Fluorescence Quenching of Surfactant Suspended Single-Walled Carbon Nanotubes in Response to Glucose. *ACS Nano* **2012**, *6*, 819−830.
(40) Beyene, A. G.; Alizadehmojarad, A. A.; Dorlhiac, G.; Goh, N.; Streets, A. M.; Král, P.; Vuković, L.; Landry, M. P. Ultralarge Modulation of Fluorescence by Neuromodulators in Carbon Nanotubes Functionalized with Self-Assembled Oligonucleotide Rings. *Nano Lett.* **2018**, *18*, 6995−7003.
(41) Crochet, J.; Clemens, M.; Hertel, T. Quantum Yield Heterogeneities of Aqueous Single-Wall Carbon Nanotube Suspensions. *J. Am. Chem. Soc.* **2007**, *129*, 8058−8059.
(42) Pan, J.; Li, F.; Choi, J. H. Single-Walled Carbon Nanotubes as Optical Probes for Bio-Sensing and Imaging. *J. Mater. Chem. B* **2017**, *5*, 6511−6522.
(43) Kong, B.; Seog, J. H.; Graham, L. M.; Lee, S. B. Experimental Considerations on the Cytotoxicity of Nanoparticles. *Nanomedicine* **2011**, *6*, 929−941.
(44) Zauner, W.; Farrow, N. A.; Haines, A. M. R. Vitro Uptake of Polystyrene Microspheres: Effect of Particle Size, Cell Line and Cell Density. *J. Controlled Release* **2001**, *71*, 39−51.
(45) Pacheco, P.; White, D.; Sulchek, T. Effects of Microparticle Size and Fc Density on Macrophage Phagocytosis. *PLoS One* **2013**, *8*, No. e60989.
(46) Foroozandeh, P.; Aziz, A. A. Insight into Cellular Uptake and Intracellular Trafficking of Nanoparticles. *Nanoscale Res. Lett.* **2018**, *13*, 339.
(47) Tian, F.; Cui, D.; Schwarz, H.; Estrada, G. G.; Kobayashi, H. Cytotoxicity of Single-Wall Carbon Nanotubes on Human Fibroblasts. *Toxicol. In Vitro* **2006**, *20*, 1202−1212.
(48) Naumov, A. V.; Ghosh, S.; Tsyboulski, D. A.; Bachilo, S. M.; Weisman, R. B. Analyzing Absorption Backgrounds in Single-Walled Carbon Nanotube Spectra. *ACS Nano* **2011**, *5*, 1639−1648.
(49) Shanthi, C.; Porpatham, R. K.; Pappa, N. Image Analysis for Particle Size Distribution. *Int. J. Eng. Technol.* **2014**, *6*, 1340−1345.
(50) Jena, P. V.; Gravely, M.; Cupo, C.; Safaee, M. M.; Roxbury, D.; Heller, D. A. Hyperspectral Counting of Multiplexed Nanoparticle Emitters in Single Cells and Organelles. *ACS Nano* **2022**, *16*, 3092−3104.
(51) Walkey, C. D.; Olsen, J. B.; Guo, H.; Emili, A.; Chan, W. C. W. Nanoparticle Size and Surface Chemistry Determine Serum Protein Adsorption and Macrophage Uptake. *J. Am. Chem. Soc.* **2012**, *134*, 2139−2147.
(52) Fratoddi, I.; Venditti, I.; Cametti, C.; Russo, M. V. The Puzzle of Toxicity of Gold Nanoparticles. The Case-Study of HeLa Cells. *Toxicol. Res.* **2015**, *4*, 796−800.
(53) Kaba, S.; Egorova, E. Vitro Studies of the Toxic Effects of Silver Nanoparticles on HeLa and U937 Cells. *Nanotechnol., Sci. Appl.* **2015**, *8*, 19.
(54) Renero-Lecuna, C.; Iturrioz-Rodríguez, N.; González-Lavado, E.; Padín-González, E.; Navarro-Palomares, E.; Valdivia-Fernández, L.; García-Hevia, L.; Fanarraga, M. L.; González-Legarreta, L. Effect of Size, Shape, and Composition on the Interaction of Different Nanomaterials with HeLa Cells. *J. Nanomater.* **2019**, *2019*, 1−11.
(55) Pan, A.; Jakaria, M. G.; Meenach, S. A.; Bothun, G. D. Radiofrequency and Near-Infrared Responsive Core−Shell Nanostructures Using Layersome Templates for Cancer Treatment. *ACS Appl. Bio Mater.* **2019**, *3*, 273−281.
(56) Liu, Z.; Davis, C.; Cai, W.; He, L.; Chen, X.; Dai, H. Circulation and Long-Term Fate of Functionalized, Biocompatible Single-Walled Carbon Nanotubes in Mice Probed by Raman Spectroscopy. *Proc. Natl. Acad. Sci. U.S.A.* **2008**, *105*, 1410−1415.
(57) Gravely, M.; Safaee, M. M.; Roxbury, D. Biomolecular Functionalization of a Nanomaterial to Control Stability and Retention within Live Cells. *Nano Lett.* **2019**, *19*, 6203−6212.
(58) Huotari, J.; Helenius, A. Endosome Maturation. *EMBO J.* **2011**, *30*, 3481−3500.
(59) Ke, N.; Wang, X.; Xu, X.; Abassi, Y. A. The xCELLigence System for Real-Time and Label-Free Monitoring of Cell Viability. In *Mammalian Cell Viability*; Springer, 2011; pp 33−43.
(60) Roxbury, D.; Jena, P. V.; Williams, R. M.; Enyedi, B.; Niethammer, P.; Marcet, S.; Verhaegen, M.; Blais-Ouellette, S.; Heller, D. A. Hyperspectral Microscopy of Near-Infrared Fluorescence Enables 17-Chirality Carbon Nanotube Imaging. *Sci. Rep.* **2015**, *5*, 14167.

https://doi.org/10.1021/acsami.2c02238
ACS Appl. Mater. Interfaces XXXX, XXX, XXX−XXX